Variation of PEM Fuel Cell Physical Parameters with Current: Impedance Spectroscopy Study

Tatyana Reshetenko[a,*,z] and Andrei Kulikovsky[b,c,*,z]

[a]*Hawaii Natural Energy Institute, University of Hawaii, Honolulu, Hawaii 96822, USA*
[b]*Institute of Energy and Climate Research, Electrochemical Process Engineering (IEK-3), Research Center "Juelich", D-52425 Juelich, Germany*
[c]*Research Computing Center, Moscow State University, 119991 Moscow, Russia*

Experimental impedance spectra of a segmented PEM fuel cell are fitted using a numerical impedance model based on the transient macrohomogeneous equations for the cathode side. Dependence of the cell transport and kinetic parameters on the current density is reported in the range from 50 to 400 mA cm^{-2}. The largest variation (growth by an order of magnitude) exhibit the cathode catalyst layer proton conductivity σ_p and oxygen diffusivity. Moreover, σ_p exhibits a stepwise change at the current density $\simeq$ 200 mA cm^{-2}. This jump could lead to formation of current-carrying and current-free zones over the cell surface. Recent experimental data (*JES*, **156**, B301 (2009)) show that this configuration is indeed realized in PEMFCs with the high- and low-current density zones under the channel and rib, respectively.

 [DOI: 10.1149/2.0981609jes]

Manuscript submitted April 14, 2016; revised manuscript received May 13, 2016. Published July 20, 2016.

Impedance spectra of a polymer electrolyte membrane (PEM) fuel cell contain important information on the cell transport and kinetic parameters. This information is, however, hidden in small (sometimes tiny) variations of the spectrum shape. Deciphering of spectra requires modeling.

A standard approach to experimental spectrum processing is based on heuristic composition of an equivalent transmission line (TL), which has a spectrum close to the experimental one (see e.g. Refs. 1–4). This approach, however, does not give relations between the TL elements and the physical parameters of the cell. A more recent distribution of relaxation times (DRT) technique[5,6] allows to construct an equivalent circuit rather than to guess it. This technique is based on integral transform of the cell impedance back into the time domain, which enables accurate resolution of frequency-dependent impedance peaks. These peaks could be associated with standard impedance elements and in this way an equivalent circuit consisting of connected in series elements is generated. A key advantage of the DRT technique is accurate resolution of almost merged peaks in the frequency dependence of impedance. However, the physical nature of these peaks is beyond the scope of the DRT method *per se*.

Concurrently, many efforts have been made to develop physical impedance models.[7–18] Basically, any transient physical model for the cell performance can be transformed into impedance model by means of linearization and Fourier-transform of the model equations. In general, the resulting linear system of equations for the perturbation amplitudes has to be solved numerically. Fitting impedance model to the experimental spectra enables, in principle, determination of all the physical parameters appearing in the model equations. However, a fitting procedure involving numerical solution of a boundary-value problem is slow. To the best of our knowledge, so far, this kind of procedure has been realized in the classic work of Springer et al.[7] only.

Analytical solutions of the aforementioned boundary-value problems can be obtained for sufficiently small cell currents, typically less than 100 mA cm^{-2}.[19–23] The respective impedance models are fast for massive least-squares processing of experimental spectra.[20,21,23,24] However, in the most interesting range of the cell current density j_0 between 0.1 A cm^{-2} and 1 A cm^{-2} these models do not work and the dependence of cell parameters on j_0 remains poorly understood.

In this work, we perform least-squares fitting of impedance spectra measured at the cell currents between 50 mA cm^{-2} and 400 mA cm^{-2}. The fitting algorithm is based on the numerical impedance model, which is obtained from the standard system of macrohomogeneous equations for the cathode catalyst layer (CCL) performance, coupled to the oxygen transport equation in the gas diffusion layer (GDL). The main result of this work is the dependence of the Tafel slope, double layer capacitance, CCL proton conductivity and of the oxygen diffusivity on the cell current density. The numerical impedance model below is two to three orders of magnitude slower, than the low-current analytical models.[19–23] Nonetheless, fitting of a single spectrum takes about an hour on a standard PC, and hence the model is suitable for research purposes and, in particular, for rationalizing the dependency of the cell parameters on j_0.

Experimental

The experiments have been performed using segmented cell system developed at Hawaii Natural Energy Institute (HNEI) following the ideas proposed in Refs. 25–28. The segmented cell system consists of the cell hardware, the custom designed current transducer system, the data acquisition device and the single cell test station (Figure 1a). The system allows the data collection from 10 current channels in a high (standard) current mode and from 10 channels in a low current mode. The standard current mode enables measurement of segment current densities up to 2 A cm^{-2}. The low current mode yields measurement of current up to 50 mA cm^{-2}, which is typical for electrochemical diagnostics. The modules are operated separately, i.e., simultaneously only 10 channels in the high or low current modes can be used.

The segmented flow field of a cell consists of ten segments forming a continuous path along ten parallel serpentine channels (Figure 1b). Each segment is equipped with its own current collector and GDL and it has an area of 7.6 cm^2. The catalyst layer is not segmented. The ratio of the CCL thickness to the segment characteristic in-plane size is about 10^{-3}, which means, that the layer through-plane resistance is much less than the in-plane resistance. In other words, currents in the CCL flow mainly in the through-plane direction and segmentation of the electrode is not needed. The segmented hardware is applicable to either the anode or the cathode. The same channel designs are used for both the segmented and the standard flow fields (the reactant streams were arranged in a co-flow configuration, and segment 1 is the inlet segment).

HNEI's system has closed loop Hall sensors (Honeywell CSNN 191) for current detection and a National Instrument PXI data acquisition system operating on HNEI developed LabView programs, which allows us to perform simultaneous measurements of spatial electrochemical impedance spectroscopy (EIS), linear sweep voltammetry

*Electrochemical Society Member.
[z]E-mail: tatyanar@hawaii.edu; A.kulikovsky@fz-juelich.de

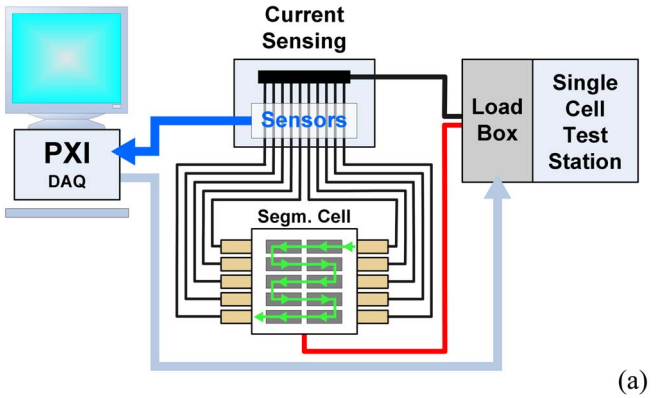

(a)

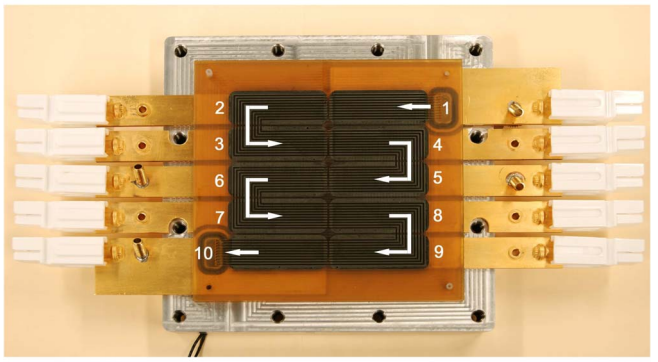

(b)

Figure 1. (a) Segmented cell measurement setup (reproduced with permission from Ref. 29) and (b) segmented cathode flow field including current collector plates.

and cyclic voltammetry.[29] The data sampling frequency of the PXI is 1 MHz, sufficient for measuring simultaneous responses from 10 segments. The diagnostic tool is operated as a single fuel cell using a GRandalytics test station. Standardized testing protocols were used for recording spatially resolved data. All experiments were carried out under galvanostatic control of the total cell current. Thus, the segments' current, voltage and the cell voltage responses were recorded by the segmented cell hardware and the data acquisition system at a fixed overall cell load. This minimizes any impact of the segmented cell system on the segments' performance. Such operation of the segmented cell system also mimics the real conditions, as only the total current is controlled, whereas the local current may vary between the segments. For the present cell design, the segments' voltage and the cell voltage responses were the same due to relatively small electrode area and high electric conductivity of the electrodes.

The cell was operated with commercially available 100 cm^2 catalyst coated membrane from Gore with the thickness of 40–42 μm. The thickness of the reinforced membrane itself was 16–18 μm. The Pt/C loading of the anode and cathode electrodes was 0.4 mg_{Pt} cm^{-2}. Sigracet 25 BC (thickness 235 μm, 80% porosity) was used as the anode and cathode gas diffusion layers (GDLs). 25 BC consists of carbon paper substrate and microporous layer with the thickness of 40–45 μm. Segmented GDL was used on the cathode side, whereas a uniform GDL was applied at the anode. The total active area of membrane/electrode assembly (MEA) was 76 cm^2. The gasket material was made of Teflon, with the thicknesses of 125 μm for the anode and cathode.

The segmented cell was assembled, conditioned and tested by recording the polarization curve and impedance. The anode/cathode conditions were hydrogen/air at 2/9.5 stoichiometry, 100/50% relative humidity and back pressure of 150 kPa. The cell temperature was 80°C. The frequency range for the EIS measurements was 0.05 Hz to 10 kHz and the amplitude of the sinusoidal current perturbation corresponded to the amplitude of the cell voltage response of 10 mV or lower. The impedance spectra were collected at the cell current density in the range of 50–400 mA cm^{-2}. The current perturbation signal was 0.5 A for current densities of 50 and 100 mA cm^{-2}, and 1 A for 200 to 400 mA cm^{-2}. Impedance spectra were measured simultaneously from 10 channels and from the whole cell. The perturbation signal is fed to the analog input of the electronic load where it is overlaid on the DC point of operation set via the test station GPIB. A master clock generator synchronizes the perturbation generator and all analog input channels. The perturbation generator signal frequency is controlled by the master clock generator and is equal to 10 times its frequency. Under these conditions, the sinusoidal output signal is smoother with smaller incremental steps, while keeping the multichannel acquisition within hardware specifications. In addition, the use of the same clock for all devices allows the system to sweep both generation and acquisition frequencies by sweeping the master clock only, without changing any other parameters, and maintaining the same sample density per period for all frequencies. The measured current and voltage DC and AC components are separated, and the amplitude and phase information is extracted from the sinusoidal sub-signal.

Impedance Model

The impedance model follows from the system of transient equations for the CCL performance:

$$C_{dl}\frac{\partial \eta}{\partial t} + \frac{\partial j}{\partial x} = -2i_*\left(\frac{c}{c_{ref}}\right)\sinh\left(\frac{\eta}{b}\right) \quad [1]$$

$$j = -\sigma_p\frac{\partial \eta}{\partial x} \quad [2]$$

$$\frac{\partial c}{\partial t} - D_{ox}\frac{\partial^2 c}{\partial x^2} = -\frac{2i_*}{4F}\left(\frac{c}{c_{ref}}\right)\sinh\left(\frac{\eta}{b}\right) \quad [3]$$

Here C_{dl} is the double layer volumetric capacitance (F cm^{-3}), η is the ORR overpotential, t is time, j is the local proton current density, x is the distance from the membrane through the CCL depth, i_* is the volumetric exchange current density (A cm^{-3}), c is the local oxygen concentration, c_{ref} is its reference concentration, b is the Tafel slope, σ_p is the CCL proton conductivity, D_{ox} is the effective oxygen diffusion coefficient in the CCL.

Eq. 1 is the proton charge conservation equation, Eq. 2 is the Ohm's law relating the proton current density to the gradient of overpotential, and Eq. 3 is the oxygen transport equation in the CCL with the Fick's law of diffusion. Detailed discussion of Eqs. 1–3 is given in Ref. 30. Substitution of Eq. 2 into Eq. 1 gives the diffusion-type equation for the overpotential. Linearization and Fourier-transform of the resulting system leads to the following pair of linear equations for the small-amplitude perturbations of overpotential η^1 and oxygen concentration c^1 (see Ref. 30 for details):

$$\varepsilon^2\frac{\partial^2 \tilde{\eta}^1}{\partial \tilde{x}^2} = \sinh(\tilde{\eta}^0)\tilde{c}^1 + (\tilde{c}^0\cosh\tilde{\eta}^0 + i\tilde{\omega})\tilde{\eta}^1 \quad [4]$$

$$\varepsilon^2\tilde{D}_{ox}\frac{\partial^2 \tilde{c}^1}{\partial \tilde{x}^2} = (\sinh\tilde{\eta}^0 + i\tilde{\omega}\mu^2)\tilde{c}^1 + \tilde{c}^0\cosh(\tilde{\eta}^0)\tilde{\eta}^1 \quad [5]$$

where the superscripts 0 and 1 mark the steady-state solution and the amplitude of a small harmonic perturbation, respectively,

$$\varepsilon = \sqrt{\frac{\sigma_p b}{2i_* l_t^2}}, \quad \mu = \sqrt{\frac{4Fc_{ref}}{C_{dl}b}} \quad [6]$$

and the following dimensionless variables are used

$$\tilde{x} = \frac{x}{l_t}, \quad \tilde{t} = \frac{t}{t_*}, \quad \tilde{\eta} = \frac{\eta}{b}, \quad \tilde{j} = \frac{j}{j_p}, \quad \tilde{c} = \frac{c}{c_{ref}}$$
$$\tilde{D}_{ox} = \frac{D_{ox}}{D_*}, \quad \tilde{Z} = \frac{Z\sigma_p}{l_t}, \quad \tilde{\omega} = \omega t_* \quad [7]$$

Here $\omega = 2\pi f$ is the angular frequency of the applied signal,

$$t_* = \frac{C_{dl} b}{2 i_*}, \quad j_p = \frac{\sigma_p b}{l_t}, \quad D_* = \frac{\sigma_p b}{4 F c_{ref}} \qquad [8]$$

are the scaling parameters for time, current density, and diffusion coefficient, respectively.

The system of Equations 4, 5 subject to the boundary conditions

$$\tilde{\eta}^1(1) = \tilde{\eta}^1_1, \quad \left.\frac{\partial \tilde{\eta}^1}{\partial \tilde{x}}\right|_{\tilde{x}=1} = 0 \qquad [9]$$

$$\left.\frac{\partial \tilde{c}^1}{\partial \tilde{x}}\right|_{\tilde{x}=0} = 0, \quad \tilde{c}^1(1) = \tilde{c}^1_b(1) \qquad [10]$$

The first of Eq. 9 fixes the perturbation amplitude of applied signal at $\tilde{x} = 1$; the second one means zero proton current at the CCL/GDL interface. Eq. 10 express zero oxygen flux through the membrane and continuity of the oxygen concentration at the CCL/GDL interface, respectively. Here, $\tilde{c}^1_b$ is the perturbation amplitude of the oxygen concentration in the GDL. The equation for $\tilde{c}^1_b$ is obtained from the oxygen mass balance in the GDL, which in the dimensionless variables 7 has the form

$$\mu^2 \frac{\partial \tilde{c}_b}{\partial \tilde{t}} - \varepsilon^2 \tilde{D}_b \frac{\partial^2 \tilde{c}_b}{\partial \tilde{x}^2} = 0 \qquad [11]$$

where $\tilde{c}_b = c_b / c_{ref}$ and $\tilde{D}_b = D_b / D_*$ are the dimensionless oxygen concentration and the effective oxygen diffusion coefficient in the GDL, respectively.

Eq. 11 is linear and hence the equation for the oxygen concentration perturbation amplitude $\tilde{c}^1_b$ is

$$\varepsilon^2 \tilde{D}_b \frac{\partial^2 \tilde{c}^1_b}{\partial \tilde{x}^2} = \mathrm{i}\mu^2 \tilde{\omega} \tilde{c}^1_b, \qquad [12]$$

The boundary conditions for this equation are

$$\tilde{D}_b \left.\frac{\partial \tilde{c}^1_b}{\partial \tilde{x}}\right|_{\tilde{x}=1} = \tilde{D}_{ox} \left.\frac{\partial \tilde{c}^1}{\partial \tilde{x}}\right|_{\tilde{x}=1}, \quad \tilde{c}^1_b(1 + \tilde{l}_b) = 0 \qquad [13]$$

where l_b is the GDL thickness. The first condition means continuity of the oxygen flux at the CCL/GDL interface, and the second one expresses zero concentration disturbance in the channel. The latter condition holds under high stoichiometry of the oxygen flow in the channel.

Eq. 12 and the system 4, 5 are linked through the boundary conditions at the CCL/GDL interface, Eqs. 10, 13. Solving Eq. 12 and setting $\tilde{x} = 1$ in the solution, we get

$$\tilde{c}^1_b(1) = -\frac{\tanh\left(\mu \tilde{l}_b \sqrt{\mathrm{i}\tilde{\omega}/(\varepsilon^2 \tilde{D}_b)}\right)}{\mu \sqrt{\mathrm{i}\tilde{\omega} \tilde{D}_b / \varepsilon^2}} \tilde{D}_{ox} \left.\frac{\partial \tilde{c}^1}{\partial \tilde{x}}\right|_{\tilde{x}=1}. \qquad [14]$$

With this, the second of Eq. 10 transforms into the Robin-type boundary condition:

$$\tilde{c}^1(1) + \frac{\tanh\left(\mu \tilde{l}_b \sqrt{\mathrm{i}\tilde{\omega}/(\varepsilon^2 \tilde{D}_b)}\right)}{\mu \sqrt{\mathrm{i}\tilde{\omega} \tilde{D}_b / \varepsilon^2}} \tilde{D}_{ox} \left.\frac{\partial \tilde{c}^1}{\partial \tilde{x}}\right|_{\tilde{x}=1} = 0 \qquad [15]$$

The static shapes $\tilde{\eta}^0$ and $\tilde{c}^0$ are solutions to the dimensionless steady-state version of the system 1–3:

$$\varepsilon^2 \frac{\partial^2 \tilde{\eta}^0}{\partial \tilde{x}^2} = \tilde{c}^0 \sinh \tilde{\eta}^0, \quad \tilde{\eta}^0(0) = \tilde{\eta}^0_0, \quad \left.\frac{\partial \tilde{\eta}^0}{\partial \tilde{x}}\right|_{\tilde{x}=1} = 0 \qquad [16]$$

$$\varepsilon^2 \tilde{D}_{ox} \frac{\partial^2 \tilde{c}^0}{\partial \tilde{x}^2} = \tilde{c}^0 \sinh \tilde{\eta}^0, \quad \left.\frac{\partial \tilde{c}^0}{\partial \tilde{x}}\right|_{\tilde{x}=0} = 0, \quad \tilde{c}^0(1) = 1 - \frac{\tilde{j}_0}{\tilde{j}_{\lim}} \qquad [17]$$

where $j_{\lim} = 4 F D_b c_{ref} / l_b$. The static cell current density $\tilde{j}^0$ is related to $\tilde{c}^0$ and $\tilde{\eta}^0$ by

$$\tilde{j}_0 = \frac{1}{\varepsilon^2} \int_0^1 \tilde{c}^0 \sinh \tilde{\eta}^0 \, d\tilde{x}$$

This equation is obtained by integration of the proton charge conservation equation

$$\varepsilon^2 \frac{\partial \tilde{j}}{\partial \tilde{x}} = -\tilde{c}^0 \sinh \tilde{\eta}^0$$

over $\tilde{x}$ from 0 to 1. Note that iterations are needed, as Eq. 17 contains $\tilde{j}_0$ in the boundary condition.

Numerical solution of the system of Equations 4, 5 with the boundary conditions 9, 15, and the first of Eq. 10 yields the amplitude of ovepotential perturbation $\tilde{\eta}^1(\tilde{x})$. Note that the oxygen transport in the GDL is included into the system for the CCL 4, 5 through the boundary condition 15. Finally, the impedance of the system "CCL+GDL" is calculated according to

$$\tilde{Z} = -\left.\frac{\tilde{\eta}^1}{\partial \tilde{\eta}^1 / \partial \tilde{x}}\right|_{\tilde{x}=0} \qquad [18]$$

Results and Discussion

The code for experimental impedance spectra fitting was developed in Maple environment. The complex-valued Eqs. 4, 5 have been converted into the system for the real and imaginary part of the perturbation amplitudes. The equations have been solved using a numerical form of the Maple procedure *dsolve*, which integrates numerically the boundary-value system of equations. An option for automatic construction of the adaptive numerical mesh has been used. The fitting itself was based on the matrix form of the built-in Maple procedure *NonlinearFit*. The static shapes of $\tilde{\eta}^0$ and $\tilde{c}^0$ have been updated in a loop after every tenth iteration with *NonlinearFit*. The total number of *NonlinearFit* iterations for fitting of a single spectrum is around one hundred, which results in the CPU time of about one hour on a standard PC.

The code has been tested by fitting the low-current experimental spectrum of a high-temperature PEM fuel cell measured in Ref. 16. The results of fitting are compared to those from the analytical impedance model[21] in Figure 2. The analytical impedance is a solution of the system of Equations 4, 5 under the assumption that the static shapes $\tilde{c}^0$ and $\tilde{\eta}^0$ are constant through the CCL depth. This solution is valid provided that the cell current density is sufficiently small; for further details see Ref. 21. As can be seen, analytical and numerical models give almost indistinguishable fitting curves and both the models nicely fit the experiment (Figure 2). The analytical and numerical fitting parameters from both the models are very close to each other (Table I). However, the numerical model above was not able to capture the oxygen diffusion coefficient in the GDL (Table I); the reason for this failure is discussed below.

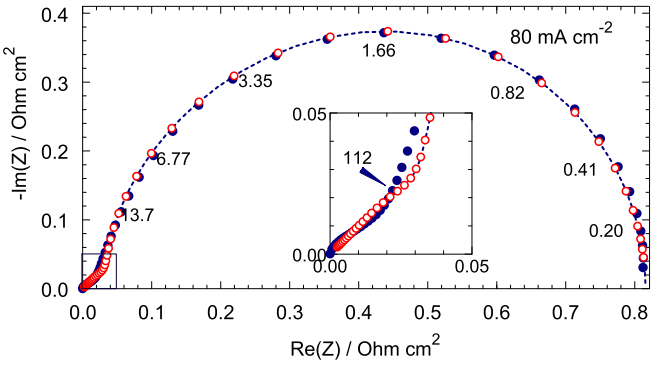

Figure 2. Filled circles – experimental impedance spectrum of an HT–PEMFC.[16] Open circles – fitted numerical model (the points corresponding to the experimental frequency values are shown), dashed line – fitted analytical model.[21] The inset shows the high-frequency part of the spectra. Numbers at the experimental points indicate the respective frequencies (Hz).

Table I. Fitting parameters for the spectrum in Figure 2 from analytical model[21] (dashed curve in Figure 2) and from the present numerical model (open circles in Figure 2).

	Analytical model	Numerical model
Tafel slope b, mV	48.8	47.3
CCL proton conductivity σ_p, Ω^{-1} cm^{-1}	0.0495	0.0496
DL capacitance C_{dl}, F cm^{-3}	20.5	20.8
CCL oxygen diffusivity D_{ox}, cm^2 s^{-1}	$1.93 \cdot 10^{-4}$	$1.78 \cdot 10^{-4}$
GDL oxygen diffusivity D_b, cm^2 s^{-1}	0.0290	–

Next, the numerical model has been fitted to our experimental spectra. The high-frequency points with the positive imaginary part of impedance have been discarded, as these points represent the impedance of cables. A trivial shift of the impedance spectra due to the membrane ohmic resistance has been removed, i.e., the spectra have been shifted to the left along the real axis to ensure that in the most high-frequency point, the real part of impedance is zero.

Figure 3 shows the numerical model (solid lines) fitted to the experimental spectra of the whole fuel cell (points) for the current densities from 50 mA cm^{-2} to 400 mA cm^{-2}. In the low-frequency range, the cell impedance exhibits an arc (Figure 3). We attributed this arc to the finite stoichiometry λ of the air flow ($\lambda = 9.5$ in our experiments).[22,31] As this effect is not described in the model, this arc has been excluded from fitting by setting the weights of the arc points to zero. Further, the experimental spectra exhibit a high-frequency capacitive feature, which distorts the straight 45°-line due to the proton transport in the CCL. This feature is specific to PEMFCs, and it has been observed in Refs. 32, 33 and also in our previous works.[23,24] The nature of this feature yet is not fully understood; suggested explanations include the frequency-dependent redistribution of reaction rate between the primary and secondary pores in the catalyst layer[34] and non-uniformity of the CCL transport properties along the CCL thickness.[35] Here, this feature has been excluded from fitting by setting the weights of the respective impedance points to zero. The LF boundary for the excluded points is indicated in Figure 3 by arrows. Thus, only the points between the leftmost and the rightmost arrows in Figure 3 have been used for fitting. Note that accurate resolution of the straight HF line is not necessary, as the position itself of the main faradaic arc determines the CCL proton conductivity.[36] Further, The HF feature discussed above is independent of the cell current density.[23,24,32,33] Thus, though the absolute value of the CCL proton conductivity could be affected by the neglect of the ohmic resistivity R_f associated with this feature, this neglect does not change the shape of σ_p dependence on the cell current discussed below. Note that at small cell currents of 50 to 100 mA cm^{-2}, σ_p resulted from fitting (0.01–0.02 Ω^{-1} cm^{-1}) agrees well with the literature data, which suggests that R_f is small as compared to the CCL proton resistance.

The spectra acquired from segments 1–9 have been fitted in the same manner. The spectra from segment 10 have not been fitted due to a high noise in the experimental data. This noise is seemingly caused by accumulation of liquid water in the last segment, close to the air channel outlet. Essentially, the air flow stoichiometry in our experiments was large ($\lambda = 9.5$), and hence the spectra from individual segments must be almost the same. In other words, ten spectra for each current density provide good statistics for the fitting parameters.

The dependence of fitting parameters on the cell current density is shown in Figure 4. In every frame of Figure 4, ten points for each current density correspond to nine segments (1–9), plus one point for the whole cell. As can be seen, the Tafel slope exhibits moderate growth from 32 mV to 43 mV (74 to 99 mV/decade) as the cell current increases from 50 to 400 mA cm^{-2} (Figure 4a). This growth can be attributed to the following effect. Pt nanoparticle is a multifaceted object with the facets having different crystallographic surface structure. With the growth of overpotential, the preferential

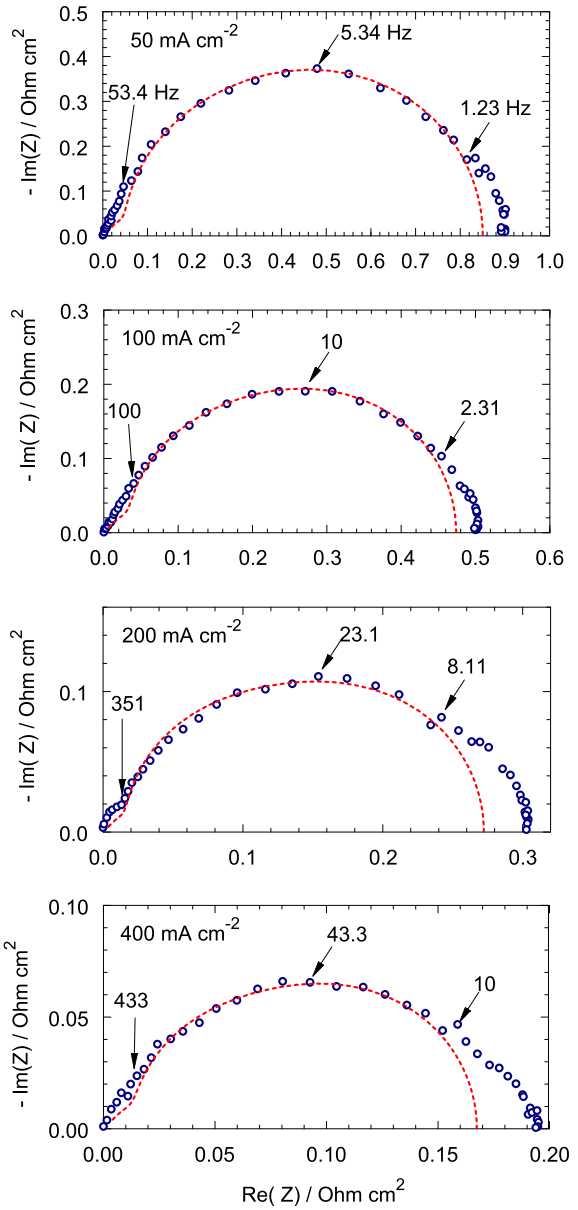

Figure 3. Points – the experimental spectra of the whole fuel cell for the indicated cell current density, dashed lines – fitted model. Numbers at the experimental points indicate the respective frequencies (Hz). Note that only the points between the leftmost and the rightmost arrows have been used for fitting.

location of ORR may move from one type of facets to another, which explains a slight increase in the Tafel slope in Figure 4a. Note that the fitting returns a pure "kinetic" value of the Tafel slope; the doubling of apparent Tafel slope due to transport effects in the CCL[37] is taken into account by the model equations.

The largest variation (nearly by an order of magnitude) with the cell current exhibit the CCL proton conductivity (Figure 4b) and oxygen diffusivity (Figure 4d). Note that these parameters are effective, mean-field values for the given CCL and operating conditions. In particular, we do not specify the physical pathways for the diffusion of oxygen, which may be transported through parallel channels in gaseous and dissolved forms. In other words, the model does not resolve oxygen diffusion mechanisms in the CCL.

The CCL proton conductivity σ_p grows with the cell current from 0.01 Ω^{-1} cm^{-1} to 0.07 Ω^{-1} cm^{-1} (Figure 4b). This growth could be attributed to accumulation of liquid water in the CCL with the increase

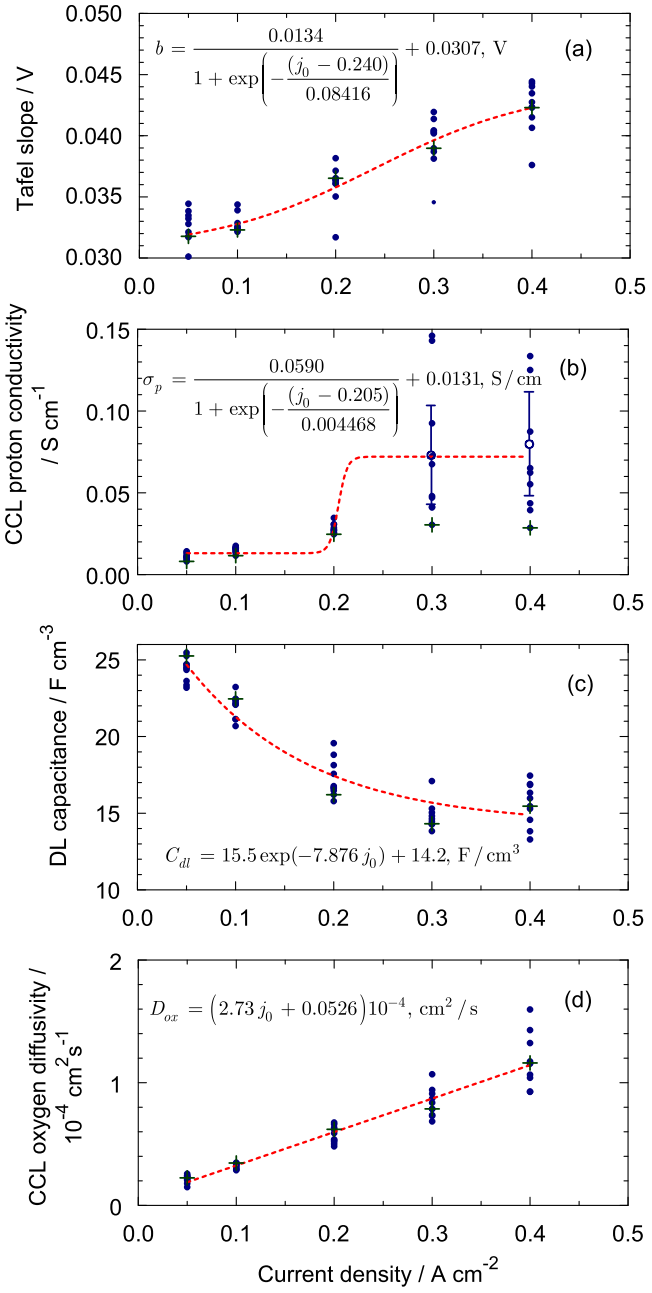

Figure 4. The dependence of cell parameters on current density resulted from fitting. Crosses indicate the values obtained from the fitting of the whole cell spectra. The equations show some reasonable fits (dashed curves). In the equations, j_0 should be in A cm^{-2}.

in current. Note, however, that the fitting function for the dependence $\sigma_p(j_0)$

$$f(j_0) = \frac{p}{1+\exp\left(-\frac{j_0-j_*}{m}\right)} + q, \quad \text{fitting parameters: } p, q, j_*, m$$

exhibits a step change at the current density of 205 mA cm^{-2} (Figure 4b). This step exhibits a strong change of the ionomer proton transport properties in the CCL. The same function used for fitting the dependence $b(j_0)$ yields a much more smooth curve (Figure 4a). Note that the point of symmetry for $b(j_0)$ is at $j_* = 240$ mA cm^{-2}, which is close to $j_* = 205$ mA cm^{-2} in Figure 4b. This is another argument in favor of the conjecture on reconstruction of the Nafion structure at the current density around 200 mA cm^{-2}. With the growth of the cell current, the noise in the experimental impedance spectra increases (Figure 3), which leads to rather large spread of the σ_p values (Figure 4b). However, the 95%-confidence intervals in Figure 4b show that the σ_p jump is statistically significant.

The oxygen diffusion coefficient in the CCL exhibits linear sixfold growth from $0.2\cdot10^{-4}$ cm^2 s^{-1} at 50 mA cm^{-2} to $1.2\cdot10^{-4}$ cm^2 s^{-1} at 400 mA cm^{-2} (Figure 4d). The origin of this growth is not quite clear. It could be explained by growing with the current spatial separation of ionomer and void phases in the CCL volume. The ionomer phase expands as the amount of liquid water increases, thereby increasing the gaseous pressure. This could lead to formation of local paths for gaseous transport in the CCL. The oxygen transport in the gas phase is nearly three orders of magnitude faster, than in the liquid phase, and formation of void paths would result in a strong increase in the total rate of the oxygen transport.

Another possible mechanism of D_{ox} growth is as following. The first step in the chain of the ORR events is oxygen adsorption on the catalyst surface. Since the rate of this adsorption is not taken into account in the total ORR rate (the right side of Eq. 1), in the present model, the adsorption process contributes to the effective CCL oxygen diffusivity. At high cell potentials, Pt surface is severely "poisoned" by oxides, and it gets "clean" as the cell potential decreases.[38,39] Thus, one may expect growth of O_2 adsorption rate with the cell current, which in our model translates into increasing D_{ox}. Similar mechanism has been discussed in Ref. 40 where the oxygen transport effects in a low-Pt loaded electrodes have been studied.

Last but not least, liquid water partly covers the Pt active surface, thereby lowering the double layer capacitance C_{dl} of the electrode by a factor of two (Figure 4c). The variation in C_{dl} is, however, not as dramatic, as increase in σ_p and D_{ox}.

The model above was not able to capture the GDL oxygen diffusivity. Possible reason is that the model employs numerical calculation of the Jacobian. The derivatives of the merit function over the fitting parameters are calculated using a simple finite-difference scheme, which may be not sufficiently accurate for D_b determination. Note that the low-current analytical model[21] used for the present model validation employs analytical relations for the respective derivatives and it gives quite a reasonable value of the GDL transport parameter (Table I).

Figure 5 shows the variation of CCL parameters with the position along the air channel for the smallest and largest current densities used in the experiment. The shape of the Tafel slope simply shifts along the b-axis as a whole as the cell current increases (Figure 5a). This suggests, that the variation of b with the segment number is due to uneven distribution of current between segments. Our set-up controls the total cell current, while the local segment currents may vary due to variation in the MEA parameters and uneven distribution of clamping pressure. Figure 5a also shows the Tafel slope determined from the polarization curves. As can be seen, these data agree well with low-current b calculated from the impedance measurements. This is not surprising, as the polarization curve exhibits the largest curvature (determined by b) in the low current region.

As expected, since the air flow stoichiometry is large, all the parameters in Figure 5 do not show any correlation with the segment number. For the high current, due to large noise in the experimental data (Figure 3), the spread of the points in Figure 5 is much larger than for the small cell current. The reason for this spread is seemingly gaseous bubbles transport in the porous layers of the cell. Nonetheless, the trends depicted in Figure 4 are clearly seen. It is worth noting that the present work is a first attempt to rationalize the dependency of the cell parameters on current density using a physics-based impedance model.

The stepwise dependence $\sigma_p(j_0)$ in Figure 4c could lead to formation of current-carrying and current-free zones along the MEA surface. In the current-carrying zone, the CCL proton conductivity is large, which would further support enhanced current density in this zone. In the current-free zone, the proton conductivity is low, and the total current in these zones would further be reduced. Thus, the zones of either type would be stable. Similar type of non-uniformities has been discussed in the theory of spatial pattern formation on the electrode.[41] Experiments[42,43] show that this two-zone configuration is

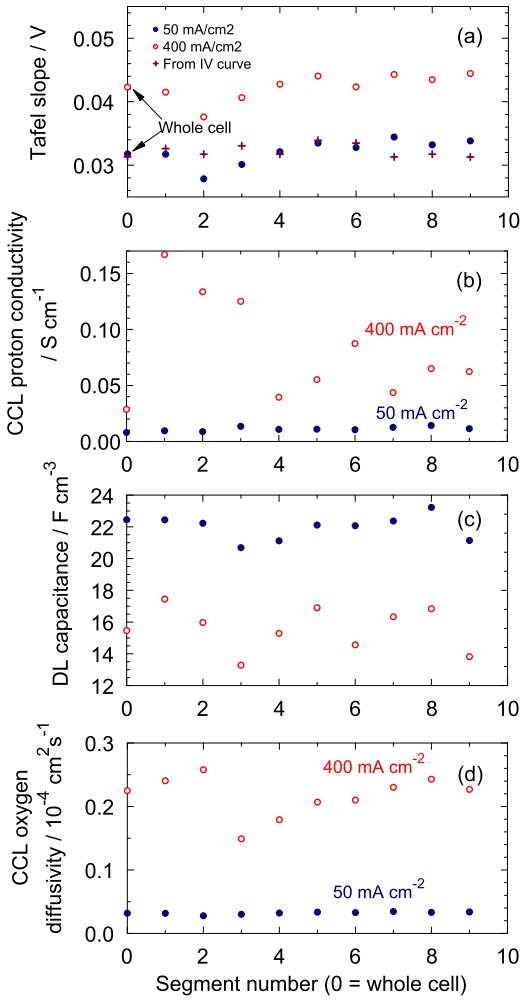

Figure 5. Fitting parameters vs channel number for the smallest (50 mA cm^{-2}) and the largest (400 mA cm^{-2}) cell current densities used in the experiment. Parameters for the whole cell are indicated at zero segment. Crosses in (a) indicate the Tafel slope obtained from the polarization curve in the range of current densities from 0 to 200 mA cm^{-2}.

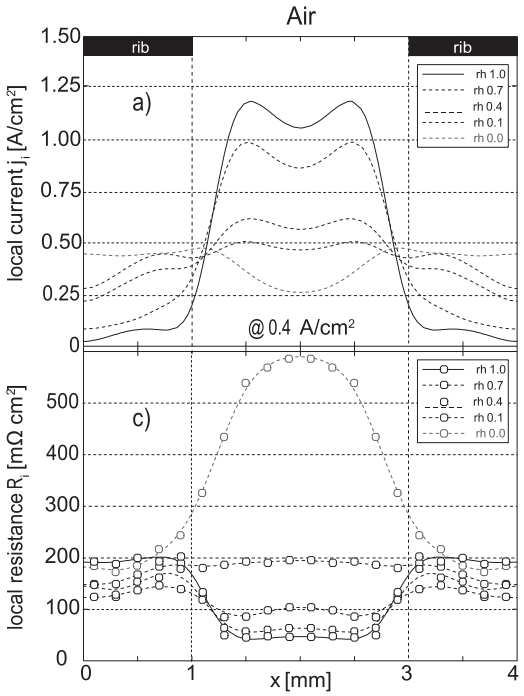

Figure 6. The experimental distributions of (a) local current density and (b) membrane resistance under the air channel and rib in a PEMFC for indicated values of the relative humidity (rh) of the anode and cathode streams. The local current is reconstructed from measured potential at the CCL/GDL interface. Reproduced with permission from Ref. 43.

indeed realized in PEM fuel cells. Figure 6 reprinted from Ref. 43 shows the measured distribution of local current density under the channel and rib for different relative humidities (rh) of the anode and cathode streams. As can be seen, at high rh, which corresponds to our experimental conditions, the distribution of local current exhibits this two-zone configuration, with the high-current zone located under the air channel and low-current zone under the rib (Figure 6a). Of particular interest is Figure 6b, which shows that the membrane resistance is lowest under the channel. This is another indication of a strong reconstruction of the Nafion structure in the current-carrying zone. Liquid water usually accumulates under the rib,[44] and one would expect a highest membrane conductivity also under the rib. However, the largest conductivity exhibits the membrane domain under the channel (Figure 6b), where the high proton current flows. The two-zone effect is, therefore, most likely due to structural charges in the current-carrying bulk Nafion and in the Nafion phase of the CCL, rather than due to mere increase in the Nafion water content. Some indications that the proton current improves Nafion through-plane conductivity have been reported by Aleksandrova et al. (see Figure 2b in Ref. 45). In a recent work, Hiesgen et al.[46] reported atomic force microscopy (AFM) studies of formation of ion-conducting sheets in the bulk Nafion under the constant current conditions. In the pristine membrane, these sheets do not exist. Though the dynamics of current sheets formation has not been studied, one may assume that the number of sheets, or their size increases with the current density in the membrane; this could explain the growth of σ_p with the current.

Finally, we note that the key parameters determining the regime of CCL operation are the characteristic current densities for the proton j_p and oxygen j_D transport: $j_p = \sigma_p b/l_t$, $j_D = 4FD_{ox}c_1/l_t$ where c_1 is the oxygen concentration at the CCL/GDL interface. In a well-designed electrode, the ratios j_p/j_0 and j_D/j_0 should exceed unity. Calculation with the fitting curves from Figure 3 shows that these ratios are, indeed, larger than unity.

Conclusions

Experimental impedance spectra measured with segmented PEM fuel cell have been fitted using the physical impedance model. The model is numerical and it allows us to calculate the cell impedance at arbitrary working current density. The model is obtained from the system of transient conservation equations for the cathode catalyst layer and the gas diffusion layer. Nonlinear least-squares fitting has been performed in Maple environment.

The main result of this work is the dependence of fitting parameters on the cell current density in the range of currents from 50 mA cm^{-2} to 400 mA cm^{-2}. The ORR Tafel slope exhibits moderate growth from 32 to 43 mV in this range, while the double layer capacitance decreases by a factor of two, from 25 to 15 F cm^{-3}. Most interesting is the dramatic (nearly by an order of magnitude) growth of the catalyst layer proton conductivity from 0.01 Ω^{-1} cm^{-1} to 0.07 Ω^{-1} cm^{-1}, and of the oxygen diffusivity from $0.2 \cdot 10^{-4}$ cm^2 s^{-1} to $1.2 \cdot 10^{-4}$ cm^2 s^{-1}. Moreover, σ_p changes rapidly at the current density of about 200 mA cm^{-2}. The growth of σ_p and D_{ox} with the cell current suggests a strong change of ionomer and void cluster properties in the CCL at higher currents. Another possible mechanism of D_{ox} growth is "cleaning" of Pt surface from the oxides as the cell potential decreases. In our model, this cleaning translates into increase in the effective D_{ox}. The jump of σ_p could cause instability leading to formation of current-carrying and current-free zones over the cell surface. Recent experiments[43] show

that this two-zone configuration is indeed realized in PEMFC with the high- and low-current density zones under the channel and rib, respectively.

Acknowledgments

T. Reshetenko is grateful to funding from US Office of Naval Research (N00014-11-1-0391), US Army Research Office (W911NF-15-1-0188) and the Hawaiian Electric Company for ongoing support of the Hawaii Sustainable Energy Research Facility.

List of Symbols

~	Marks dimensionless variables
b	Tafel slope $b = RT/\alpha F$, V
C_{dl}	Double layer volumetric capacitance, F cm^{-3}
c	Oxygen molar concentration in the CCL, mol cm^{-3}
c_b	Oxygen molar concentration in the GDL, mol cm^{-3}
c_{ref}	Oxygen molar concentration in the channel, mol cm^{-3}
D_{ox}	Effective oxygen diffusion coefficient in the CCL, cm^2 s^{-1}
D_b	Effective oxygen diffusion coefficient in the GDL, cm^2 s^{-1}
F	Faraday constant, C mol^{-1}
f	Regular frequency, Hz
j_D	Characterisitc cell current density for oxygen transport in the CCL, Eq. 8, A cm^{-2}
j	Local proton current density in the CCL, A cm^{-2}
j_0	Local cell current density, A cm^{-2}
j_p	Characterisitc cell current density for proton transport in the CCL, Eq. 8, A cm^{-2}
i	Imaginary unit
i_*	Volumetric exchange current density, A cm^{-3}
l_b	Gas-diffusion layer thickness, cm
l_t	Catalyst layer thickness, cm
t	Time, s
t_*	Characteristic time of double layer charging, s, Eq. 8
x	Coordinate through the cell, cm
Z	Total impedance of the cathode side, Ω cm^2

Greek

α	ORR transfer coefficient
ε	Newman's dimensionless reaction penetration depth, Eq. 6
η	Local ORR overpotential (positive by convention), V
μ	Dimensionless parameter, Eq. 6
σ_p	CCL ionic conductivity, Ω^{-1} cm^{-1}
ω	Angular frequency ($\omega = 2\pi f$), s^{-1}

Subscripts

0	Membrane/CCL interface
1	CCL/GDL interface
b	GDL
t	Catalyst layer
$*$	Characteristic value

Superscripts

0	Steady-state value
1	small-amplitude perturbation

References

1. S. Arisetty et al., *J. Electrochem. Soc.*, **159**, B455 (2012).
2. M. S. Kondratenko, M. O. Gallyamov, and A. R. Khokhlov, *Int. J. Hydrogen Energy*, **37**, 2596 (2012).
3. A. C. Okafor and H.-M. C. Mogbo, *J. Fuel Cell Sci. Techn.*, **9**, 011006 (2012).
4. J. Kim, J. Lee, and B. H. Cho, *IEEE Trans. Ind. Electronics*, **60**, 5086 (2013).
5. H. Schichlein, A. C. Müller, M. Voigts, A. Krügel, and E. Ivers-Tiffée, *J. Appl. Electrochem.*, **32**, 875 (2002).
6. Y. Zhang, Y. Chen, M. Yan, and F. Chen, *J. Power Sources*, **283**, 464 (2015).
7. T. E. Springer, T. A. Zawodzinski, M. S. Wilson, and S. Gottesfeld, *J. Electrochem. Soc.*, **143**, 587 (1996).
8. Y. Bultel, L. Genies, O. Antoine, P. Ozil, and R. Durand, *J. Electroanal. Chem.*, **527**, 143 (2002).
9. F. Jaouen and G. Lindbergh, *J. Electrochem. Soc.*, **150**, A1699 (2003).
10. Q. Guo and R. E. White, *J. Electrochem. Soc.*, **151**, E133 (2004).
11. Y. Bultel, K. Wiezell, F. Jaouen, P. Ozil, and G. Lindbergh, *Electrochimica Acta*, **51**, 474 (2005).
12. D. Gerteisen, A. Hakenjos, and J. O. Schumacher, *J. Power Sources*, **173**, 346 (2007).
13. A. A. Franco, P. Schott, C. Jallut, and B. Maschke, *Fuel Cells*, **7**, 99 (2007).
14. M. Cimenti, D. Bessarabov, M. Tam, and J. Stumper, *ECS Transactions*, **28**, 147 (2010).
15. I. A. Schneider, M. H. Bayer, and S. von Dahlen, *J. Electrochem. Soc.*, **158**, B343 (2011).
16. O. Shamardina, M. S. Kondratenko, A. V. Chertovich, and A. A. Kulikovsky, *Int. J. Hydrogen Energy*, **39**, 2224 (2014).
17. B. P. Setzler and T. F. Fuller, *J. Electrochem. Soc.*, **162**, F519 (2015).
18. C. Bao and W. G. Bessler, *J. Power Sources*, **278**, 675 (2015).
19. A. A. Kulikovsky and M. Eikerling, *J. Electroanal. Chem.*, **691**, 13 (2013).
20. A. A. Kulikovsky, *Electrochimica Acta*, **147**, 773 (2014).
21. A. A. Kulikovsky, *J. Electrochem. Soc.*, **162**, F217 (2015).
22. A. Kulikovsky and O. Shamardina, *J. Electrochem. Soc.*, **162**, F1068 (2015).
23. T. Reshetenko and A. Kulikovsky, *J. Electrochem. Soc.*, **163**, F238 (2016).
24. T. Reshetenko and A. Kulikovsky, *J. Electrochem. Soc.*, **162**, F627 (2015).
25. S. J. C. Cleghorn, C. R. Derouin, M. S. Wilson, and S. Gottesfeld, *J. Appl. Electrochem.*, **28**, 663 (1998).
26. J. Stumper, S. A. Campbell, D. P. Wilkinson, M. C. Johnson, and M. Davis, *Electrochimica Acta*, **43**, 3773 (1998).
27. G. Bender, M. S. Wilson, and T. A. Zawodzinski, *J. Power Sources*, **123**, 163 (2003).
28. C. Wieser, A. Helmbold, and E. Gulzow, *J. Appl. Electrochem.*, **30**, 803 (2000).
29. T. V. Reshetenko, G. Bender, K. Bethune, and R. Rocheleau, *Electrochimica Acta*, **56**, 8700 (2011).
30. A. A. Kulikovsky, *J. Electroanal. Chem.*, **669**, 28 (2012).
31. I. A. Schneider, S. A. Freunberger, D. Kramer, A. Wokaun, and G. G. Scherer, *J. Electrochem. Soc.*, **154**, B383 (2007).
32. M. Keddam, C. Rakotomavo, and H. Takenouti, *J. Power Sources*, **161**, 920 (2006).
33. D. Malevich, E. Halliop, B. A. Peppley, J. G. Pharoah, and K. Karan, *J. Electrochem. Soc.*, **156**, B216 (2009).
34. H. Nara, S. Tominaka, T. Momma, and T. Osaka, *J. Electrochem. Soc.*, **158**, B1184 (2011).
35. D. Gerteisen, *J. Electrochem. Soc.*, **162**, F1431 (2015).
36. A. A. Kulikovsky, *J. Electroanal. Chem.*, **738**, 108 (2014).
37. A. A. Kulikovsky, *Electrochimica Acta*, **55**, 6391 (2010).
38. H. Xu, R. Kunz, and J. M. Fenton, *Electrochem. Solid State Lett.*, **10**, B1 (2007).
39. E. L. Redmond, B. P. Setzler, F. M. Alamgir, and T. F. Fuller, *Phys. Chem. Chem. Phys.*, **16**, 5301 (2014).
40. J. P. Owejan, J. E. Owejan, and W. Gu, *J. Electrochem. Soc.*, **160**, F824 (2013).
41. K. Krischer, Principles of temporal and spatial pattern formation in electrochemical systems, in *Modern Aspects of Electrochemistry*, edited by B. E. Conway, J. O. Bockris, and R. E. White, volume 32, pages 1–142, Springer, New-York, 2002.
42. S. A. Freunberger, M. Reum, J. Evertz, A. Wokaun, and F. N. Büchi, *J. Electrochem. Soc.*, **153**, A2158 (2006).
43. M. Reum, S. A. Freunberger, A. Wokaun, and F. N. Büchi, *J. Electrochem. Soc.*, **156**, B301 (2009).
44. T. Rośen et al., *J. Electrochem. Soc.*, **159**, F536 (2012).
45. E. Aleksandrova, R. Hiesgen, K. A. Friedrich, and E. Roduner, *Phys. Chem. Chem. Phys.*, **9**, 2735 (2007).
46. R. Hiesgen, T. Morawietz, M. Handl, M. Corasaniti, and K. A. Friedrich, *Electrochimica Acta*, **162**, 86 (2015).